Monitoring mining-induced rock mass deformation using distributed strain monitoring based on fiber optics

Benoît Valley
Geomechanics Research Centre, MIRARCO – Mining Innovation, Sudbury, Ontario, Canada
Behrad M. Madjdabadi
Department of Civil Engineering, University of Waterloo, Waterloo, Canada
Peter K. Kaiser
CEMI, Sudbury, Ontario, Canada
Maurice B. Dusseault
Earth and Environmental Sciences Department, University of Waterloo, Waterloo, Canada

Abstract: Triggered seismicity remains one of the main geomechanics hazards that affect safety in deep mining. Mobilization or propagation of existing faults can potentially release large amounts of seismic energy that in turn may trigger rockbursts and falls of ground, threatening worker safety and generating production delays. Current modeling approaches, typically based on stress analyses, do not fully succeed in capturing such seismically triggered mechanisms as the main seismic event location may be beyond the volume of rock affected by the mining induced stress perturbation. However, the displacement field generated by the excavation process may explain the triggering of far-field seismicity. Deeper understanding of the mining-induced deformation field is the motivation for the development of mine-scale deformation monitoring techniques. Innovative deformation sensors developed for structural monitoring based on fibre optic technology allows distributed measurement of strain at high spatial sampling rates over large distances.

This paper presents the results of the testing of one of these systems in an active mining context. The system selected is based on Brillouin Optical Time Domain Analyses (BOTDA) and allows for a spatial resolution of 10 cm. It has been tested in the laboratory and installed in five boreholes piercing through an actively mined, 25 m thick, 1000 m deep, sill pillar. Benchmarking of the system against extensometer results was successful in a qualitative manner. The high spatial resolution of the fibre optic system brings valuable additional insights to rock mass deformation processes.

Theme: Mining Rock Mechanics

Keywords: Fibre optics deformation monitoring, rockburst control

1 INTRODUCTION

Currently, the single monitoring systems with high spatial and temporal resolution that are deployed in deep underground mines are seismicity and microseismicity monitoring systems. However, much of the rock mass deformation and failure process occurs occurs without generating measurable micro-seismicity. Thus, microseismic emissions can account for only a tiny portion of the total energy balance (Das and Zoback, 2011). Slow slips, low-frequency tremors, and aseismic deformation processes such as creep all are mechanisms that potentially contribute to energy transfers and releases; however, these are largely ignored because the acquired data are not processed adequately or (more likely) the necessary data are not acquired. Energy release is also largely controlled by the system loading stiffness (Salamon, 1970; van Aswegen and Mendecki, 1999; Zipf, 2001; Wiles, 2002). Stiffness cannot be measured directly, but can be evaluated by measuring the deformation (strain) induced by a known stress change. Better understanding of the stiffness and stiffness changes induced by mining could help anticipate violent failures (rockbursts) in deep mines and, more importantly, allow development of strategies to achieve controlled energy release while mining.

In view of these issues, there is a pressing need for more systematic acquisition of deformation data around deep mines. Currently, deformation monitoring in mines is mostly based on multi-point point borehole extensometers with a limited number of anchor points that are used to monitor deformations in the immediate vicinity of openings. This location is in the excavation damaged zone (e.g. Tsang *et al.* 2005), a region of elastoplastic deformation, and gives little information about the nature of the far-field elastic loading system. New type of deformation monitoring devices developed mostly for structural and civil application (e.g. pipeline, bridge, dam monitoring) and based on fibre optics system are now available that could potentially fill this gap. Various sensors exist, some offering distributed strain monitoring capability (high spatial resolution) and high (temporal) frequency capabilities.

The purpose of the work presented here is to assess the applicability of one such technology, offering distributed strain monitoring capabilities, in active mines. Findings from laboratory tests and field installations, including testing methodology, field installation procedures and initial results, are presented.

2 BACKGROUND

2.1 Distributed fibre optic based strain monitoring technique

Fibre optic sensing technology has seen rapid development over the last decade, with numerous applications for structural monitoring (e.g. Inaudi, 2003). A broad spectrum of sensors exists, from very sensitive point sensors (e.g. Fabry-Perrot, Bragg grating), averaging sensors (e.g. interferometric, microbending), to truly distributed sensors. Since the objective is to monitor far-field strains, a technology that offers truly distributed strain monitoring capability was investigated. It is based on Brillouin optical time-domain analyses (BOTDA), a sensing approach first proposed by Horiguchi and Tateda (1989). Details of the technology are given in Thévenaz (2010). It uses the temperature and strain dependency of the Brillouin frequency shift, a property of the scattered light travelling in a fibre under specific conditions. By using reflectometry, distance along the sensing fibre is obtained by processing the data initially collected in the time domain.

A system includes a read-out unit, communication fibres, and sensing fibres (Fig. 1). We used a DITEST read-out unit from Omnisens that permits a spatial

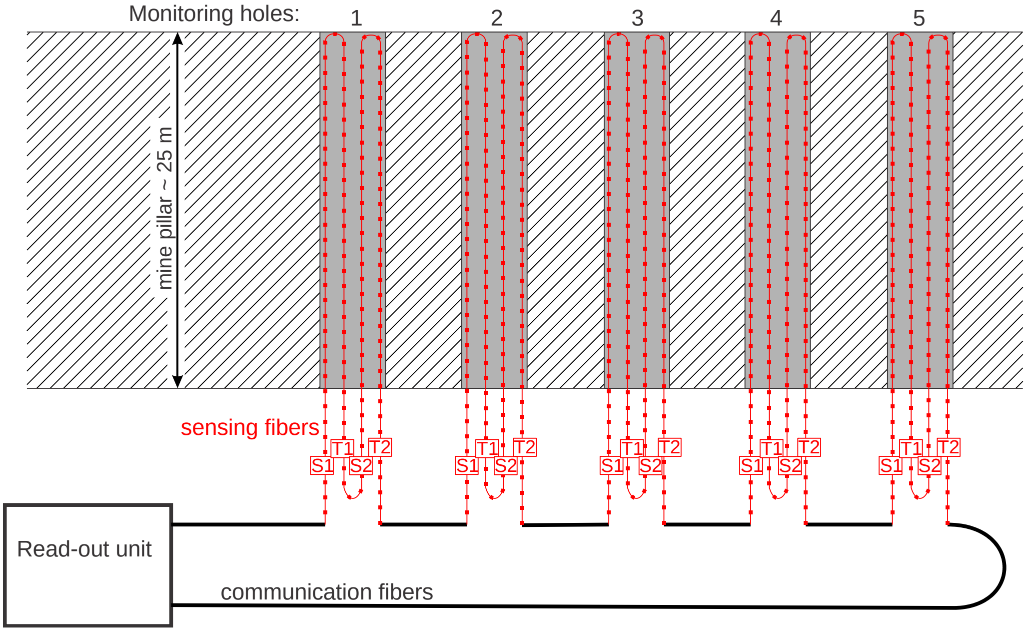

Figure 1. Schematic of the monitoring system

resolution of 0.5 m sampled at 0.1 m intervals. Brillouin frequency shift measurement ranges from 10 GHz to 13 GHz with a resolution of 0.1 MHz, which correspond to a strain resolution of ~2 με (microstrain) and temperature resolution of 0.1°C. Measurement accuracy claims from the equipment supplier are 20 με for strain and 1°C for temperature. Communication cables used are standard single mode fibre G.652 from Nexans.

The sensing fibres are provided by Smartec. They are single mode fibres embedded in a specially designed polyethylene jacket to form a sensing cable called SMARTprofile. Cable dimensions and layout are given in Fig. 2. Four fibres are embedded in the cables; two fibres, referred to as S1 and S2, are bonded within the cable jacket such that strain will be transferred to them, and two other fibres are included for temperature measurements (T1 and T2) and are located in a central conduit where they are free to slide and will not be strained. This sensing cable design offers both measurement redundancy and the possibility of performing temperature corrections.

The elastic modulus of the cable is 0.44 ± 0.015 GPa. The Brillouin frequency shift for a strain-free fibre at room temperature is about 10.8 GHz. A typical reading of a SMARTprofile cable used in this project is presented in Fig. 3. The connection schemes put the fibers in series in the following order: S1-T1-S2-T2 (see Fig. 1). Connections between S1 and T1 as well as S2 to T2 are direct splices. Connections be

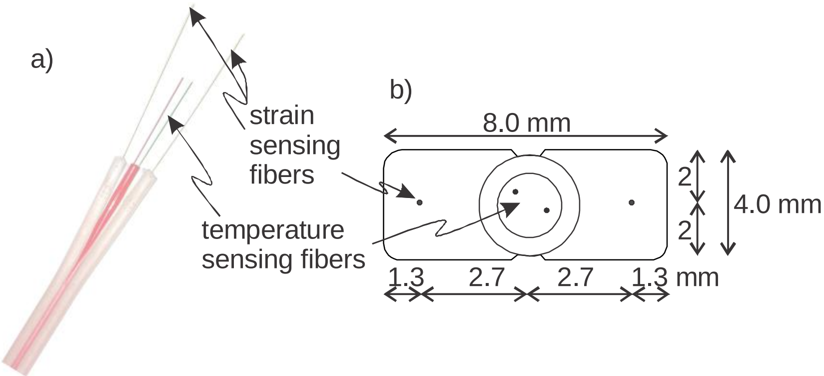

Figure 2. a) picture of the sensing cable used in this study b) section of the cable showing dimensions

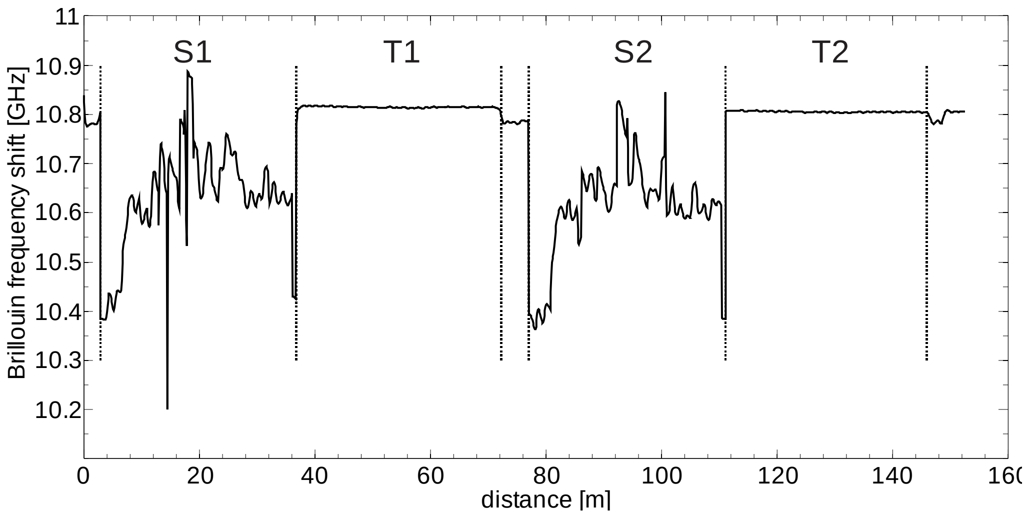

Figure 3. Typical SMARTprofile data.

tween T1 and S2 as well as at sensor ends are made using mechanical connectors (type E2000). Temperature sections of the sensor (T1 and T2) present quasi-constant Brillouin frequency shift response while strain sections of the sensor (S1 and S2) show variations in frequency in the range 10.3 to 10.9 GHz. Such variations result from the cable manufacturing process that induces strains in the bonded fibers. However, as we are solely interested in differential readings (change of frequency related to an initial reading), such variations should be unimportant as long as the frequency stays in the measurement range of the read-out unit. The recorded strain is obtained from differential readings for which each MHz change in the Brillouin frequency shift corresponds to 19.78 $\mu\varepsilon$ deformation. Similarly for the temperature, each MHz change in the Brillouin frequency shift corresponds to 0.87 °C temperature change.

2.2 Field testing context

The context of the field test is presented in Fig. 4. The situation is the early stage of extraction of a 25 m high sill pillar (Fig. 4a). Only the first five stopes of the extraction sequence (A to E) were actively mined during the monitoring period. Top sill and bottom sill development give access to the mining area (Fig. 4c). Monitoring breakthrough holes were drilled from the top sill to the bottom sill. At each location (numbered 1 to 5, Fig. 4c), two parallel holes were drilled, one for the installation of fibre optic sensing (FOS) cables and the other for the installation of multipoint borehole extensometers (MPBX). This situation gives a unique opportunity to benchmark FOS data with a comparable dataset (MPBX). In addition, optical televiewer data was

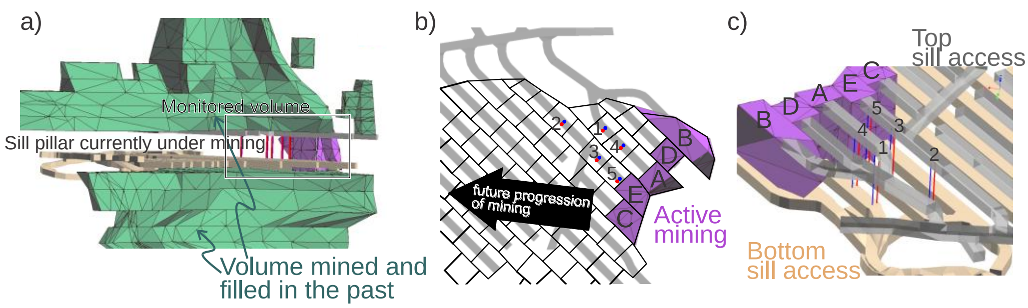

Figure 4. Overall geometry of the monitored volume a) Isometric view of the broader mining context (pillar thickness is about 25 m) b) plan view of the monitored area (typical stope size: 15m x 15 m). c) Isometric view of the monitored volume. Red: monitoring hole with fibre optic sensing cables and blue: monitoring holes with multi-point borehole extensometer.

acquired in each monitoring hole in order to provide additional context for the interpretation of the deformation datasets.

2.3 Field installation methodology

The installation layout is presented in Fig. 5a. Sensing cables were grouted in 4 inch diameter percussion-drilled holes. The cables were lowered down the hole and anchored (Fig. 5b). A device was then installed at the toe of the borehole (Fig. 5c) that had two functions: 1) centralise the sensing cable and 2) plug the hole to permit grouting. A 2 kg dead weight was attached to the cable to provide pre-tensioning. The purpose of pre-tensioning is primarily to ensure that the cable is hanging relatively straight in the borehole and also to provide some additional compressive strain reserve. A bag (0.02 m^3, i.e. about a 2.5 m column in a 4 inches diameter hole) of expanding shrinkage-free Portland cement-based grout was pumped from the toe of the borehole in order to form a solid grout plug. After a couple of days of curing of the grout plug, the hole was completely filled from the top sill with a 40 MPa grout mix made of Portland cement, sand and additives.

3 RESULTS

3.1 Lab testing results

Initial lab tests were performed on sensing cables in order to test the measurement system. Further laboratory tests that better represent the *in situ* conditions, i.e. the system sensing cable/grout/rock mass, are currently on-going. In the test results presented here, the strains were generated by dead-weight loading a cable section between two clamps.

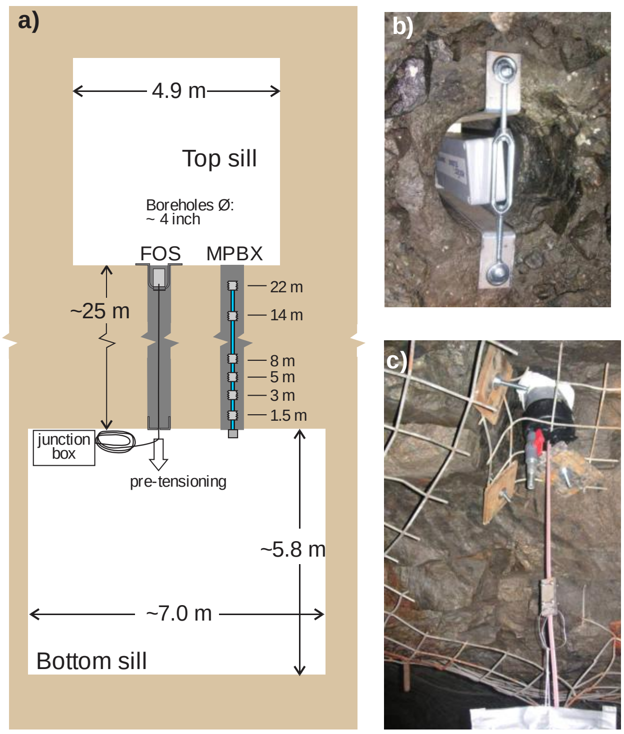

Figure 5. a) schematic of the installation layout. b) anchoring of the SMARTprofile at the top sill. The gray box is an enclosure within which S1 to T1 and S2 to T2 splices are protected c) pre-tensioning and centralising of the SMARTprofile at the bottom sill.

3.1.1 Fixed length elongation measurements

In this initial suite of tests, a one meter long section of cable was successively loaded and unloaded with increasing/decreasing weights from 0 to 5 kg. The data were acquired using a 0.1 MHz scanning step, a 5 ns pulse corresponding to a pulse length of 0.5 m, and a 0.1 m spatial resolution. The differential frequency readings, computed by subtracting the initial reading (1) for the loading steps and the final reading (12) for the unloading steps, are presented in Fig. 6a. Differential readings were filtered using an inter-quartile range filter in order to remove parasite spikes.

The differential frequency signal presents an asymmetric response spanning about 2.4 m, starting with a sharp edge (I) leading to a maximum (II) followed by a plateau value (III), a sharp decrease (IV) and a small trough (V). The distance between the two sharp edges (II and IV) spans about 1.15 m. This response is the result of the convolution of the strain applied over 1 m by the 0.5 m long laser pulse. Since both the laser pulse function and the exact applied strain profile are unknown, deconvolution cannot be applied to the signal, and the explanation of the details of the shape of the response is uncertain. It cannot be excluded that mechanical clamping at the edge of the strained interval locally induces a strain anomaly. Given these uncertainties concerning the edges of the response, it is appropriate to assume that a measure of the frequency in the center of the response (noted with horizontal black lines in Fig. 6a) is most representative of the applied strain.

Fig. 6a allows for a comparison of the response between the two redundant strain fibres (S1 and S2). The overall shape of the response is similar, but the measured frequency values differ by up to 24 MHz. Using the nominal frequency to strain conversion factor, these 24 MHz correspond to 475 microstrains, which is more than one order of magnitude larger than the claimed accuracy. Explanation of this discrepancy by

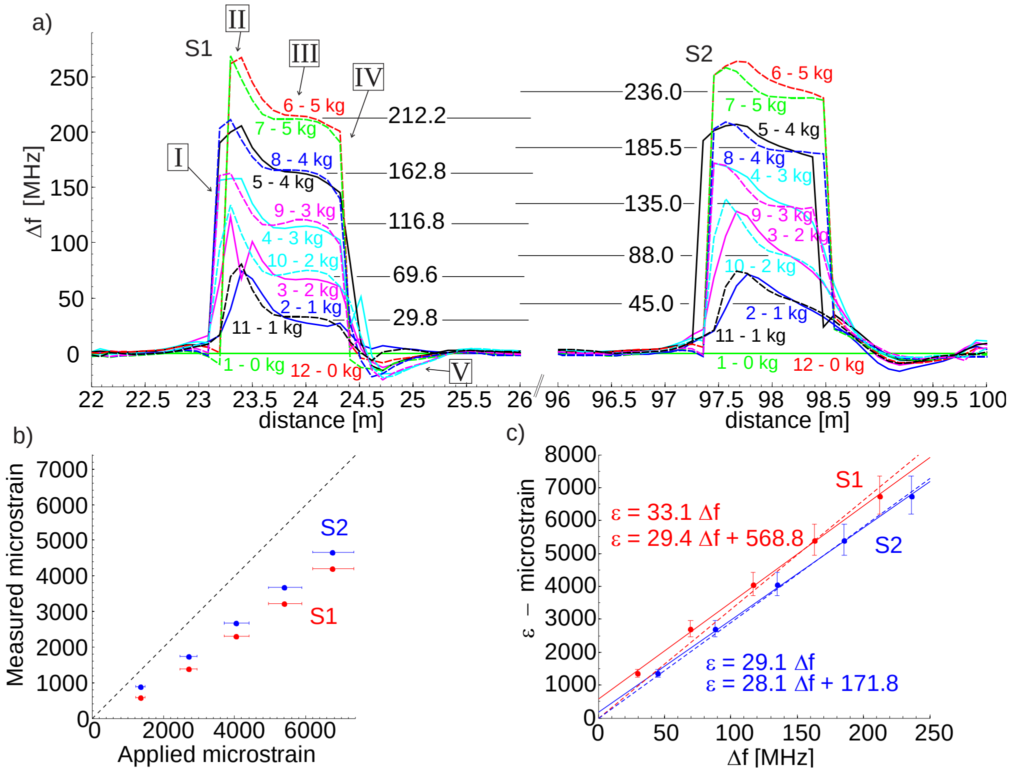

Figure 6. a) Relative Brillouin frequency shift for loading steps (1 to 6) and unloading steps (7 to 12) for strain fibers S1 and S2. b) crossplot of measured strain vs. applied strain computed based on cable nominal modulus, applied weight and cable nominal section area. c) Frequency vs. applied strain plot. Best linear fit forced through zero (dashed lines) and not forced through zero (solid line) are also included.

asymmetric loading of the cable (inducing torsion) cannot be sustained because particular care was taken to avoid torsion. Also, the large size difference between the cable diameter and the length under load implies that if any torsion was induced it should be balanced between the two fibres and average out over the monitored length. Thus, it is suggested that this discrepancy reflects the true limitation in accuracy of the system.

Concerning the suggested frequency to strain conversion factor of 19.78 με/MHz, a comparison between applied strains (computed by considering the applied load, the cable section area and the cable nominal modulus see section 2.1 and Fig. 2), and the measured strain (frequency difference multiplied by the conversion factor above) is presented in Fig. 6b. The error bars on applied strain are computed considering the uncertainty in modulus, a 10 g uncertainty on the load and a 5% uncertainty on the cable section area. Measured microstrains are significantly lower than the applied strain, suggesting that the conversion factor used could be too low. The frequency – strain plot presented in Fig. 6c suggests that a conversion factor of about 29 με/MHz would be appropriate. A significant offset of the linear trend for S1 is present, which could account for the discrepancy between the two fibres described above, although the reason for the offset is unknown.

Finally, it should be mentioned that in order to gain confidence in results such as these presented here, it is recommended that the measurement be repeated with a slightly different experimental setup. Indeed, using dead-weight loading to induce the strain is not optimal as it implies a constant load and not a constant displacement at the boundary. Time-dependent cable creep was observed due to this boundary condition, and this has definitely impacted the findings presented here.

3.1.2 Variable length elongation measurements

The effect of the length of the cable section under load on the measured response was investigated by applying a constant load of 3 kg to a decreasing cable length from 1 m to 0.01 m (results presented in Fig. 7a). Measuring parameters are otherwise the same as those described in Section 3.1.1. The measured response is compared with a theoretical response assuming the convolution of a box car signal with a box car filter (equivalent of moving average) in Fig. 7b and 7c.

Generally, the measured and theoretical responses are in acceptable agreement. The shape of the measured signal differs from the theoretical response in a manner similar to what is described in Section 3.1.1 (asymmetry). The asymmetry of the response is less pronounced for loaded sections shorter than 0.4 m. Responses for lengths under load of 0.1 m, 0.05 m and 0.01 m do not differ significantly, which implies that a signal is still clearly visible, even for load over very short section. For such short sections, the theory predicts that almost no signal should be observed. This also

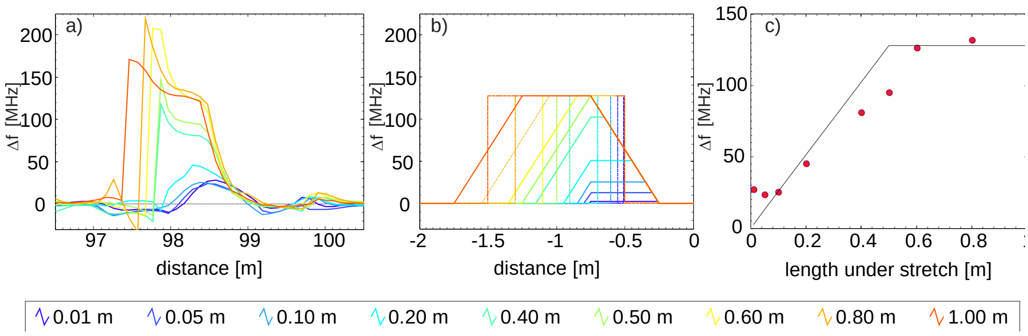

Figure 7. a) Measured response with decreasing length under stretch. b) Theoretical response (continuous lines) assuming the convolution of a box car signal (dashed lines) with a box car filter (equivalent of moving average). c) Comparison of the measured and theoretical response.

implies that the strain conversion factor (conversion from frequency to strain) for such short sections will not be valid. However, the ability to identify localized strain, albeit in a non-quantitative manner, is encouraging since localization of strain along fractures is expected to accommodate a significant part of the deformation occurring at the rock mass scale.

3.2 Field testing results

Preliminary analyses are limited to sensor installed in location 1 (see Fig. 4). The sensing cables were installed in early June, 2011, and data recording started on June 4, 2011. The general connection layout of the system is given in Fig. 1; however, the connection scheme was altered over the duration of monitoring; i.e., some of profiles were broken and the read-out unit was repeatedly reconnected. Data presented in the following sections have been carefully extracted and depth matched to ensure consistency over the entire monitoring period. Typical monitoring frequency is one record every 30 minutes (that is the time needed to scan the entire Brillouin frequency range at high resolution). However, data collection has been intermittent for most of the monitoring period due to the difficult environmental condition in which the read-out unit was located (dust and temperature). Finally, environmental control measures were successfully implemented and continuous data (i.e. one measurement every ~30 minutes) were acquired for 22 days at the end of the monitoring period (from August 30 to September 20, 2011).

3.2.1 Spatial analysis

The strain data collected from the fibre optic system at location 1 are presented in Fig. 8a. Depth 0 corresponds to the floor of the top sill and depth 25 m corresponds to the ceiling of the bottom sill (see Fig. 5). All strain data are relative to the initial reading on June 4. The data were filtered using a robust weighted linear least-squares regression algorithm in order to remove outliers (parasite spikes).

One main characteristic of the recorded signal presented in Fig. 8a is a cyclic oscillation around zero strain with a wave length of about 1.2 m and an amplitude of about 400 microstrain. These oscillations are believed to be a measurement artefact. Their origin is most probably to be found in the manufacturing process of the sensing cable that induces a highly variable and partly cyclic variation in the Brillouin frequency shift response of the unstrained cable (see Fig. 3). These variations should vanish when looking at differential readings, i.e. when subtracting the initial reading from any subsequent reading. However, if some depth mismatch exists between the initial reading and the subsequent readings, these variations will not exactly be subtracted out and a noisy response as presented in Fig. 8 will appear. The problem may have been amplified by the fact that the connection scheme has been modified over the course of the monitoring period, increasing the chance of depth mismatch.

Another characteristic of the data is an increase of the amplitude of the variations at the end of the sensor, particularly at the lower end (depth >24.5 m). These variations are interpreted to be due to temperature effects, i.e. some influence of the changing air temperature in the opening on the rock temperature directly surrounding the openings that in turn induces a thermo-elastic strain response.

A last characteristic of the data is a relatively large strain anomaly recorded by both sensing fibres at a depth of 23.5 m. This strain anomaly is interpreted as being related to movements on an existing fracture shown in Fig. 8c.

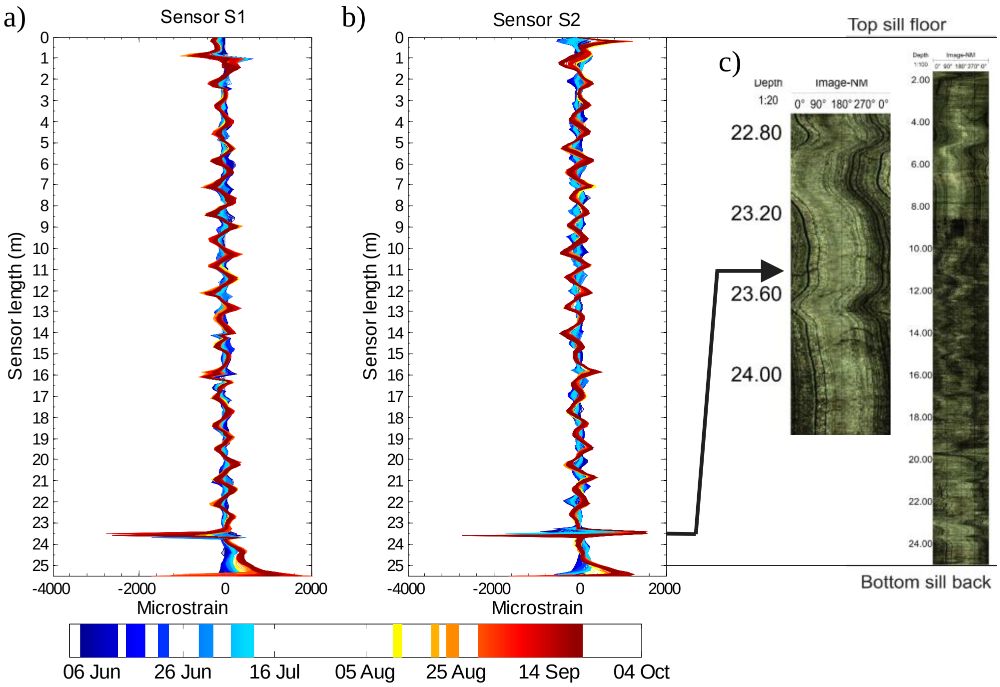

Figure 8. a) and b) Strain recording at location 1 for fiber S1 and S2 respectively. The colours correspond to the recording dates has indicated on the color bar included. White gaps on the colour bar indicate period during which no data were acquired. c) Optical televiewer image of the entire installation hole as well as zoom on the section 22.8 m to 24.3 m.

More insights are gained by looking at the displacement profiles presented in Fig. 9, which are obtained by integrating the strain data over the entire length of the pillar, assuming that the 0 m depth point is fixed. Only data from strain-sensing fibre 2 (S2) are shown because this sensor seems to provide the most consistent strain response. The data suggest an overall compressive (negative strain) trend over the entire pillar that developed very early in the monitoring period and that accumulated almost one millimetre of shortening over the entire pillar. The reason for this trend is unclear; it could be related to the monitoring artefact described above or to the curing process of the grout used to install the sensor. At 23.5 m, i.e. the depth of the fracture-related strain anomaly, a step in the displacement profile can be observed. This step is absent from the record in June (blue in Fig. 9) and develops in the August record (red in Fig. 9) to reach a magnitude of 0.25 mm. The most probable explanation for this step is the downward movement of a small block of rock in the roof of the bottom sill delineated by the fracture imaged in Fig. 8c.

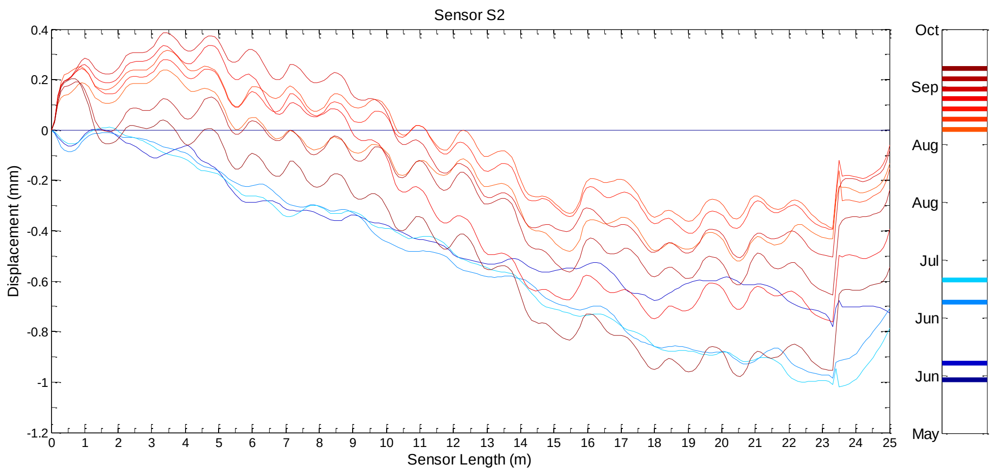

Figure 9. Cumulative displacement over length of the pillar

The data obtained by a 6-point extensometer in a parallel hole at location 1 (see Fig. 5) are shown in Fig. 10a. The head of the extensometer is located in the roof of the bottom sill (depth 0 m in Fig. 10a). Recorded displacements are displayed as a function of depth for 11 key dates over the monitoring period, assuming that the last anchor located at 22 m depth is fixed.

In order to permit direct comparisons, the fibre optics strain data at almost equivalent key dates (data availability permitting) were extracted, averaged over the entire day and integrated assuming a fixed point 3 m below the top sill floor (equivalent to the depth of the last anchor of the extensometer). These re-processed data are presented in Fig. 10b. The overall response is similar with the only significant displacement recorded over 1.5 meter in the roof of the bottom sill, at the end of the monitoring period. The fibre optic system has the advantage over the extensometer to indicate precisely where the displacement occurred, allowing identification of which fracture is actually causing the deformation. A sharp response is already visible on August 10 with the fibre optic system while the first data showing clear elongation response is on August 21 for the extensometer. However, the magnitude of the displacement differs significantly between the two systems (~2 mm for MPBX versus ~0.4 mm for FOS). A possible explanation for the difference by a factor of five is currently under detailed investigation, but it is assumed to be related to the installation setup; the compliance of the grout/fibre vs. grout/extensometer system differ, thus the deformation magnitudes should differ as well.

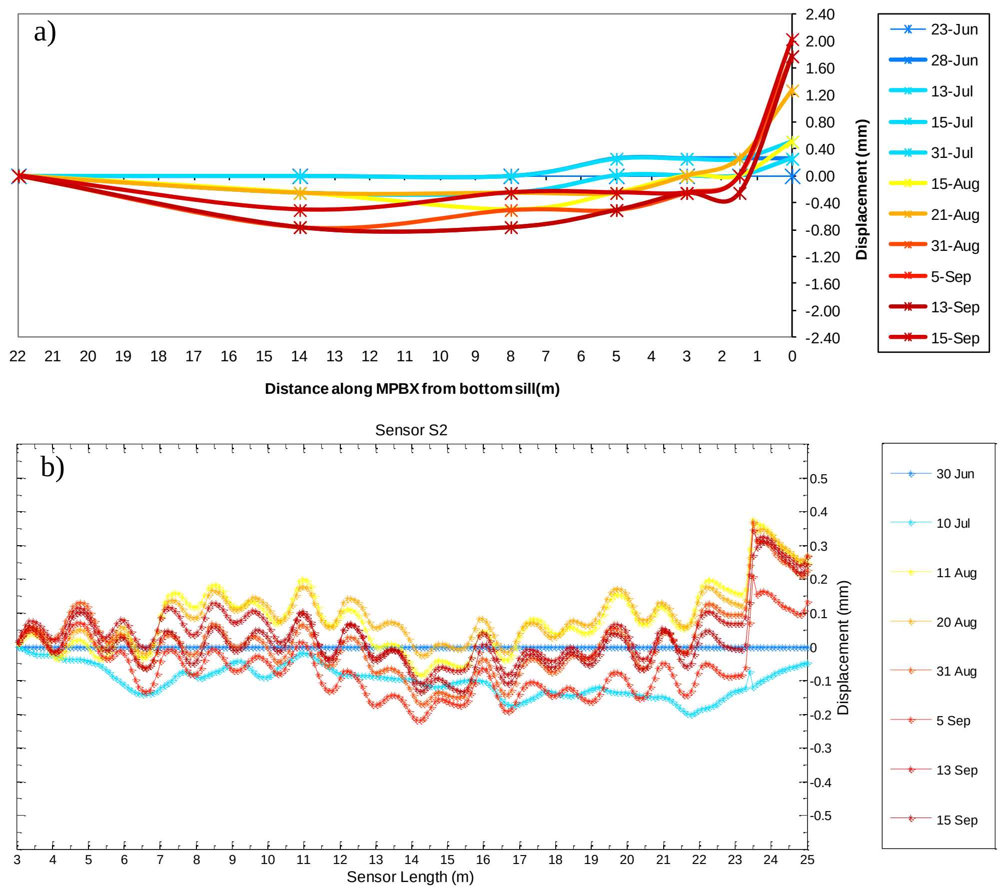

Figure 10. a) Smart MPBX results, b) FOS measurement

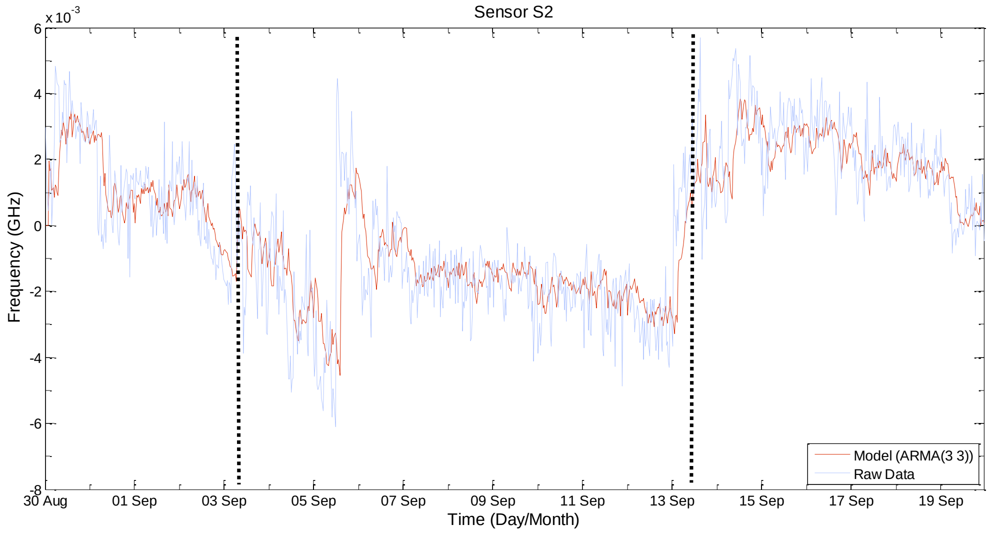

Figure 11. Time series recorded at a depth of 8m below top sill floor by the fibre optic system. The vertical dashed lines correspond to production blasts in the sensor vicinity.

3.2.2 Time series analysis

The continuous data recorded over 22 days at the end of the monitoring period at a sampling rate of 1 every ~30 minutes (864 samples over the continuous monitoring period) present a unique opportunity to study strain variations with time. A time series acquired by the fibre optic system at a depth of 8 m below the top sill floor is presented in Fig. 11 (raw data in blue). The recorded data have been resampled at a constant 5 minute interval using linear interpolation in order to facilitate the following analyses. This time series is typical of data at any depth across the pillar, except for data collected in the vicinity of the fracture-related strain anomaly described above. Variations in Brillouin frequency shift over the 22 days of record spans about 10 MHz (from -6 to +4 MHz), i.e. about 200 microstrains.

In order to verify that these variations are not just related to random noise, a lag plot is shown on Fig 12. A linear pattern can be seen on this graph generated for lag 1. This implies that the data are non-random and have a moderate to strong positive autocorrelation containing almost no outliers.

Autocorrelation plots calculated for the same data are shown in Fig. 12b and c. It can be seen that both graphs show strong autocorrelation decaying slowly to zero at large lags. This means that the data set is non-stationary, implying the presence of a trend. To make it stationary, a differencing method is used. It is worth noting that the autocorrelation plot for data coming from 20 cm above and below the fracture-related strain anomaly (not shown here) displays less dependence, which can be explained by the influence of an external factor such as slippage.

In order to remove noise from the data, an Autoregressive Moving Average (ARMA) model is fitted to the differenced data. Fig. 11 displays theses filtered data (in red), obtained by detrending the raw data and fitting an ARMA model of the order of 3 and 3 for autoregression and moving average, respectively. The model residual falls between the 95% confidence limits, ensuring that only random noise has actually been filtered out.

Generally, the time series of Fig. 11 highlight a gradual decrease of Brillouin frequency shift of about 0.5 MHz/day (~10 microstrain/day shortening). Two sharp increases in frequency of more than 4 MHz (80 microstrain elongation), occurring in less than a day, are present on September 5 and 13. The reason for the step on September 13 (dashed line in Fig. 11) is most probably because of blasting of the crown

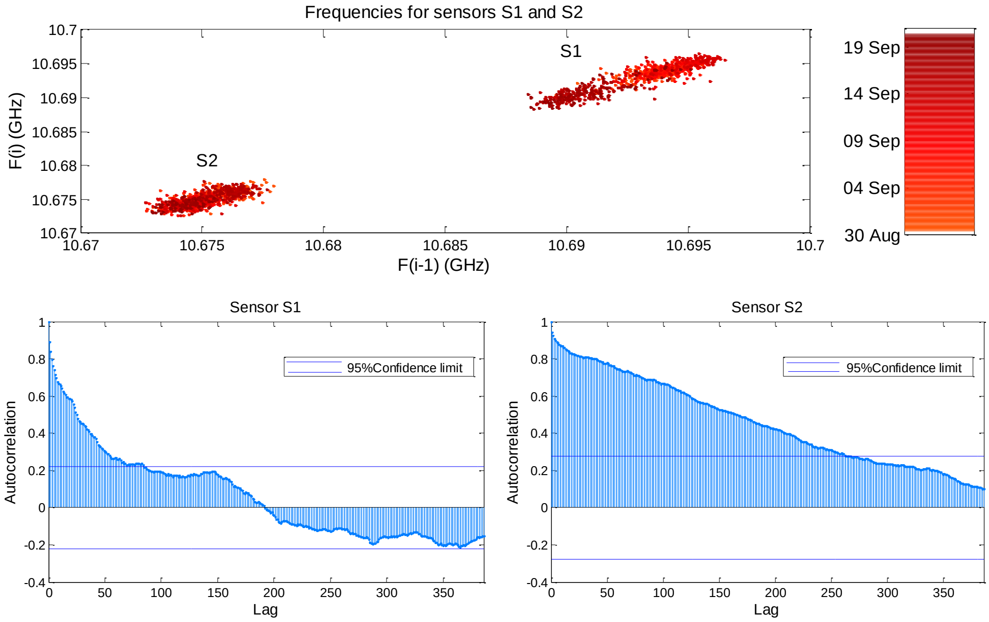

Figure 12. *a)* Lag and *b)* autocorrelation plots for frequencies measured from S1, S2

of stope C (see Fig. 4), although the details of the mechanism involved have not yet been investigated. The reason for the large step on September 5 remains unknown. A blast also took place on September 3 (dashed line in Fig. 11) in the same stope, but its effect on the strain record seems to be rather limited; it corresponds to a sharp 2 MHz local increase that does not stand out from the background noise.

In order to recognize whether there is any cyclicity in the signal, the power spectral of the differenced signal is calculated using Welch's method which is an enhanced version of a periodogram. Fig. 13 shows the power spectral density for data measured at the depth of 8 m for both stain sensors. Frequencies range from 0 to 6 (Nyquist frequency) cycles per hour. The power reaches a peak at frequencies 8.789×10^{-4} and 1.679×10^{-4} Hz, equal to almost 190 min/cycle and 100 min/cycle for sensor S1 and S2, respectively. For all depths, power spectrum peaks at frequencies ranging from 95 to 330 min/cycle exist. The reasons for these frequencies have not been elucidated yet, but since they do not correspond to any typical mining cycle, we suspect that they could be instrumentation or processing artefacts.

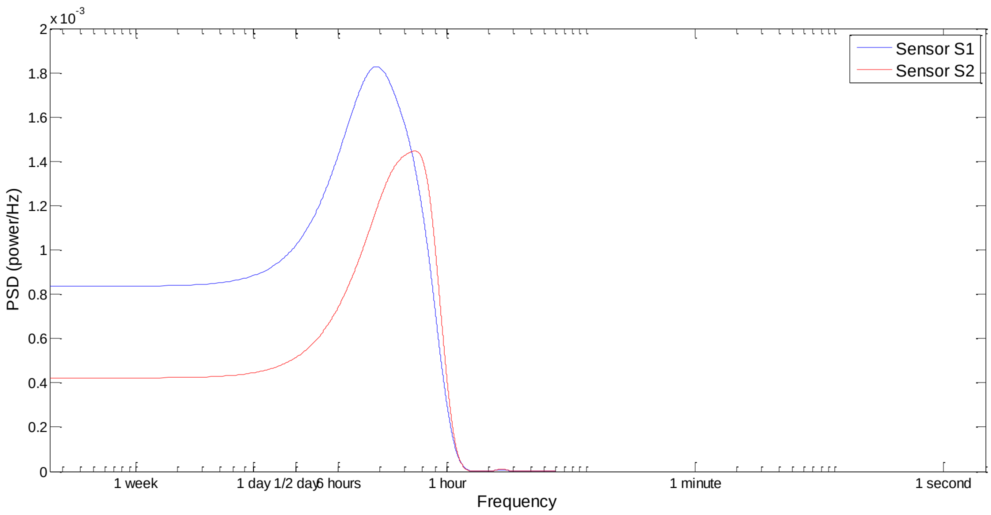

Figure 13. Power spectral density of two strain sensors for the depth of 8 m.

4 CONCLUSIONS

Better understanding of the deformation pattern around deep underground mines is needed, but currently available techniques are limited to relatively short distances and a limited number of anchor points. New distributed strain monitoring techniques based on fibre optic sensing methods developed for structural monitoring could eventually fill this gap if they can be adapted to conditions found in deep underground mines. Current testing of a fibre optic distributed deformation monitoring system both in the laboratory and in a deep underground mine setting suggests that several issues need to be resolved before reliable measurements can be obtained from fibres grouted into boreholes. While this work is still on-going, the following preliminary conclusions can be drawn:

- The laboratory results confirm that Brillouin frequency shift is linearly dependent on applied deformation. However, variability in the measured conversion factors suggest that the accuracy of 20 microstrain claimed by the equipment providers cannot be reached. In terms of absolute accuracy, a realistic target for such equipment is currently probably one order of magnitude larger, i.e. in the 200 microstrain range, but relative changes in the order of the 20 microstrain may be resolved by the system.
- Despite the fact that the laser pulse length is 50 cm long and thus strain is theoretically averaged over this length, deformation localised over only 1 cm was discernable from the background noise. This is very important because a significant part of rock mass deformation is probably accommodated by localised slip on or opening of fractures.
- The field results are encouraging as the system could cope, when properly conditioned, with the challenging environmental conditions of deep mines (heat and dust). The electronics of the read-out unit must be kept in acceptable temperature ranges. Dust did not cause problems at the read-out unit or at the connectors between successive cable sections.
- Results from *in situ* measurements processed to date suggest that the strain response measured with the fibre optic system is consistent with the deformation readings obtained from extensometers, although details and absolute magnitude differs. Laboratory testing is required to establish strain transfer factors (rock to grout to fibre). The fibre optic approach suffers from measurement artefacts that can most probably be reduced if depth matching stability between successive measurements is improved. The high spatial resolution of the fibre optic system compared to extensometer data permits deeper insight into the deformation processes, permitting identification of fracture slip or opening contributions to the measured deformation.

On-going works focuses on better processing approaches to limit artefacts and increase the signal-to-noise ratio, as well as an optimized installation methodology leading toward a higher fidelity of the rockmass deformation measurements that accounts for the sensor/grout/borehole/rockmass system compliance.

5 AKNOWLEDGMENTS

This work is funded by an equipment grant from NSERC (National Sciences and Engineering Research Council of Canada), CEMI (Centre for Excellence in Mining Innovation) by the Ontario Ministry of Research and Innovation through the SUMIT (Smart Underground Monitoring and Integrated Technology) research program. The contributions by Vale and its collaborating staff, providing access to the mine and related extensometer records, are thankfully acknowledged.

6 REFERENCES

Das, I., Zoback, M. D., 2011. Long-period, long-duration seismic events during hydraulic fracture stimulation of a shale gas reservoir. *The Leading Edge* 30(7), 778–786. doi:10.1190/1.3609093

Horiguchi, T., Tateda, M., 1989. Optical-fiber-attenuation investigation using stimulated brillouin scattering between a pulse and a continuous wave. *Opt. Lett.* 14(8), 408–410. doi:10.1364/OL.14.000408

Inaudi, D., 2003. State of the art in fiber optic sensing technology and EU structural health monitoring projects. In: First International Conference on Structural Health Monitoring and Intelligent Infrastructure. Tokyo. 8 pp.

Salamon, M., 1970. Stability, instability and design of pillar workings. *International Journal of Rock Mechanics and Mining Science & Geomechanics Abstracts* 7(6), 613–631. doi:10.1016/0148-9062(70)90022-7

Thévenaz, L., 2010. Brillouin distributed time-domain sensing in optical fibers: state of the art and perspectives. *Frontiers of Optoelectronics in China* 3(1), 13–21. doi:10.1007/s12200-009-0086-9

Tsang, C.-F., Bernier, F., Davies, C. 2005. Geohydromechanical processes in the Excavation Damaged Zone in crystalline rock, rock salt, and indurated and plastic clays—in the context of radioactive waste disposal. *International Journal of Rock Mechanics and Mining Sciences* 42(1), 109–125. doi: 10.1016/j.ijrmms.2004.08.003

van Aswegen, G., Mendecki, A. J., 1999. Mine layout, geological features and seismic hazard. *Tech. rep., SIMRAC.* 90 pp.

Wiles, T., 2002. Loading system stiffness - a parameter to evaluate rockburst potential. *In: Proceeding of the 1st international seminar on deep and high stress mining.* Australian Center for Geomechanics. 10 pp.

Zipf, R. K., 2001. Toward pillar design to prevent collapse of Room-and-Pillar mines. *In: 108th Annual Exhibit and Meeting, Society for Mining, Metallurgy, and Exploration.*11 pp.